npj | climate and atmospheric science

Article

Published in partnership with CECCR at King Abdulaziz University

https://doi.org/10.1038/s41612-026-01370-3

A novel insight into MJO predictability: initial errors can trigger a prediction barrier over the maritime continent

Check for updates

Xiaoyun Wang[1,2], Wansuo Duan[1,2] ✉ & Yuntao Wei[3] ✉

Forecasting the eastward propagation of the Madden–Julian Oscillation (MJO) across the Maritime Continent (MC) remains a significant challenge, often characterized by a rapid decline in prediction skill—a phenomenon known as the Maritime Continent prediction barrier (MC-PB). While conventional perspectives have predominantly attributed the MC-PB to model deficiencies, this study demonstrates that initial errors can also trigger a pronounced MC-PB. Furthermore, the results reveal that initial moisture errors are the dominant factor driving the growth of MJO forecast errors. By employing the Conditional Nonlinear Optimal Perturbation (CNOP) method, we identify two distinct types of initial moisture errors that are particularly prone to inducing the MC-PB for different MJO events. These initial errors exhibit distinct spatial patterns and, by modulating westward-propagating equatorial Rossby (ER) waves, disrupt MJO propagation across the MC via two physical pathways. Specifically, one type significantly decelerates MJO propagation, while the other weakens MJO intensity, both ultimately leading to the MC-PB. All these results suggest that optimizing initialization schemes provides a novel pathway for effectively alleviating the MC-PB effect and greatly improving MJO prediction level.

The Madden-Julian Oscillation (MJO) is recognized as the dominant mode governing tropical atmospheric variability on intraseasonal timescales. It is characterized by the eastward progression of large-scale convective anomalies coupled with dynamic circulation patterns[1,2]. Beyond directly modulating tropical weather anomalies, the MJO also significantly influences extratropical extreme events by exciting Rossby wave trains. The MJO affects the genesis frequency, intensity, and tracks of tropical cyclones by modulating convection, circulation, and thermodynamic conditions[3,4]. It can also induce regional floods or droughts by altering precipitation anomalies in monsoon regions and mid-latitudes[5], and increase the probability of cold surges in regions such as East Asia by affecting large-scale circulation and temperature advection[6]. Consequently, the MJO offers an important opportunity to improve subseasonal prediction of high-impact weather. Therefore, accurate MJO prediction is crucial for successful extended-range forecasting of extreme events[7–9].

The Subseasonal-to-Seasonal Prediction Project (S2S) was established in 2013 to advance forecasting capability and process understanding on subseasonal timescales[10]. Currently, numerical prediction systems from 13 operational centers and research institutes participate in this project. Defining the threshold for skillful prediction as a bivariate anomaly correlation coefficient (ACC) exceeding 0.5, the average useful forecast lead time for the Real-time Multivariate MJO (RMM)[11] index is approximately 3 weeks[12,13]. This skill remains far below the MJO's potential predictability, which is estimated to reach up to 7 weeks[13–15]. This discrepancy limits the ability to provide effective early warnings and support decision-making for disaster prevention and mitigation.

A major challenge in MJO numerical prediction is that the MJO signal weakens rapidly with increasing lead time, resulting in a sharp decline in forecast skill. This phenomenon is particularly pronounced when the MJO propagates eastward over the Maritime Continent (MC). From the perspective of forecast error growth, this manifests as a rapid increase in forecast errors as the MJO traverses the MC, resulting in the so-called "Maritime Continent prediction barrier" (MC-PB)[16–18]. The MC-PB is generally attributed to model deficiencies in representing the complex physical processes over the MC region. Specifically, many models exhibit systematic dry biases in the mean state, which hinder the maintenance of the convective envelope[13,19]. Furthermore, parameterization schemes often fail to capture the crucial multiscale interactions, particularly the rectification of the strong

[1]State Key Laboratory of Earth System Numerical Modeling and Application, Institute of Atmospheric Physics, Chinese Academy of Sciences, Beijing, China. [2]College of Marine Sciences, University of Chinese Academy of Sciences, Beijing, China. [3]Department of Atmospheric and Oceanic Sciences/Institute of Atmospheric Sciences, Fudan University, Shanghai, China. ✉e-mail: duanws@lasg.iap.ac.cn; yuntao_wei@fudan.edu.cn

diurnal cycle onto the intraseasonal scale[20–22]. Additionally, the mechanical blocking and local circulations induced by the complex land-sea distribution and steep topography are frequently poorly represented, disrupting the low-level moisture convergence essential for MJO propagation[23–25]. These limitations induce model errors that impede the accurate representation of key local processes, which in turn amplifies the resistance to MJO crossing the MC in numerical simulations[22,26].

Although the MJO serves as a critical bridge between medium-range weather forecasts and seasonal climate predictions, its forecast skill remains constrained by both model uncertainty and initial condition uncertainty[27–29]. Previous studies have shown that initial errors can contribute substantially to MJO forecast uncertainty by affecting the maintenance of convection and air-sea interaction processes[27,30,31]. In particular, Takasuka et al.[32] recently proposed that MJO propagation operates as a deterministic chaotic system, where initial state uncertainties are amplified by cross-scale nonlinearities to produce bifurcated regimes. However, it remains unclear whether initial errors can trigger the MC-PB. Addressing this question is critical for determining whether initialization strategies, such as targeted observations or data assimilation, can effectively alleviate the MC-PB effect and improve MJO forecast skill. Utilizing hindcasts from the S2S database, we first examine in this study the potential for initial errors to trigger the MC-PB. Subsequently, the Community Earth System Model, version 1 (CESM1), and the Conditional Nonlinear Optimal Perturbation (CNOP)[33] method are applied to reveal the initial error that leads to the largest forecast error and to examine whether this error can induce the MC-PB. This study aims to provide new insights for mitigating the MC-PB and improving MJO prediction skill.

Methods

Model and data

Developed by the National Center for Atmospheric Research (NCAR), CESM1 operates as a fully coupled Earth system framework consisting of interactive modules for the atmosphere, ocean, land surface, and cryosphere. Previous studies have demonstrated CESM1's robust performance in representing tropical intraseasonal variability; specifically, Li et al.[34] verified its capability to reproduce the eastward propagation of the MJO, and Richter et al.[35] reported an effective MJO prediction lead time of 27 days. Given its high simulation fidelity and competitive forecast skill, CESM1 is employed as the model for this investigation. For the details of this model on its configurations, readers can be referred to Hurrell et al.[36].

After a 200-year spin-up integration to reach an equilibrium state, CESM1 was integrated for an additional 20 years to generate data for the analysis of optimal initial errors. This study also uses multimodel hindcast datasets from the S2S database. From the 12 centers participating in Phase 2, we selected three independent hindcast datasets: the Australian Bureau of Meteorology (BoM)[37], the Institute of Atmospheric Sciences and Climate (CNR-ISAC), and the National Centers for Environmental Prediction (NCEP)[38]. Notably, the BoM prediction system uses three models (P24a, P24b, and P24c) to represent model uncertainty. To isolate the impact of initial errors and exclude the influence of model errors, only forecast data from the POAMA-P24a model were utilized. The three selected ensemble forecast systems exhibit relatively high MJO prediction skill. Crucially, these systems account for initial uncertainty solely through initial perturbations, without introducing model perturbations to represent model uncertainty. This design facilitates the investigation of the impact of initial errors on the MC-PB. Table 1 lists the key information for these three ensemble forecast systems.

Conditional nonlinear optimal perturbation (CNOP)

The state equations of atmospheric motion can be expressed as:

$$\begin{cases} \frac{\partial U}{\partial t} + F(U) = 0 \\ U|_{t=0} = U_0 \end{cases} \quad (1)$$

where U is the state vector, U_0 is its initial value, and F represents a nonlinear function. Its solution can be described as $U_T = M_T(U_0)$, where T represents the forecast time, and M is the propagator associated with Eq. (1). Assuming an initial perturbation u_0 is imposed on the initial state, its nonlinear evolution at time T can be written as: $u_T = M_T(U_0 + u_0) - M_T(U_0)$.

The above-mentioned CNOP can be solved by the following optimization problem:

$$J(u_0^*) = \max_{u_0 \in C_\delta} J(u_0) \quad (2)$$

where $J(u_0) = ||M_T(U_0 + u_0) - M_T(U_0)||_f$ is the objective function. This function quantifies the deviation from the reference state $M_T(U_0)$ induced by the initial perturbation u_0, with the norm $||\bullet||_f$. The set $C_\delta = \{u_0 \in R^n : ||u_0||_a \le \delta\}$ represents the amplitude constraint on the initial perturbation, as defined by the norm $||\bullet||_a$, and δ is a positive constant. Then the initial perturbation u_0^* in Eq. (2) is defined as the CNOP.

Note that, if the initial perturbations are regarded as initial errors, then the initial error represented by the CNOP is the one that yields the largest forecast error at forecast time T.

Results

Impact of initial uncertainty on the MC-PB

This section analyzes the three S2S ensemble hindcast datasets described in Model and Data. Since these ensemble hindcast experiments perturb only the initial conditions, they provide an ideal framework to examine the impact of initial uncertainty on the prediction of MJO propagation across the MC and to determine whether initial errors alone can trigger the MC-PB.

Given that these hindcasts cover the period from 1981 to 2013, our analysis focuses on observed MJO events during the same interval. We employ the RMM index[11] to track MJO activity. Due to its simplicity and capability to capture the coupled nature of the MJO, this index has been widely adopted for real-time monitoring and forecasting of the MJO[39]. The RMM index is calculated by applying multivariate EOF analysis to latitudinally averaged (15°S–15°N) anomalies of outgoing longwave radiation (OLR) and zonal winds at 850 hPa (U850) and 200 hPa (U200). The leading two principal components (PCs) are retained as RMM1 and RMM2. Regarding projection strategies, model anomalies in the S2S hindcast analysis are projected onto the observed EOF patterns, whereas for the CESM numerical experiments, they are projected onto the model's own internal EOFs.

MJO events were categorized by Wang et al.[40] into four distinct groups according to their zonal propagation features: fast-propagating, slow-propagating, jumping, and standing. This study focuses on continuously propagating MJO events that successfully traverse the MC. Targeting these events facilitates the examination of how initial uncertainty affects the prediction of MJO propagation characteristics over the MC. The selection criteria for these events are as follows: the RMM amplitude must be ≥1.0

Table 1 | Description of the S2S models used in this study

Model center	Model version	Reforecast period	Reforecast frequency	Time range	Ensemble size	Ensemble initial perturbation strategy
BoM	POAMA P24a	1981–2013	Six per month	Days 0–62	11	Coupled bred vectors
ISAC	GLOBO	1981–2010	Every 5 days	Days 0–32	5	lagged-ensemble technique
NCEP	CFSv2	1999–2010	Daily	Days 0–44	4	lagged-ensemble technique

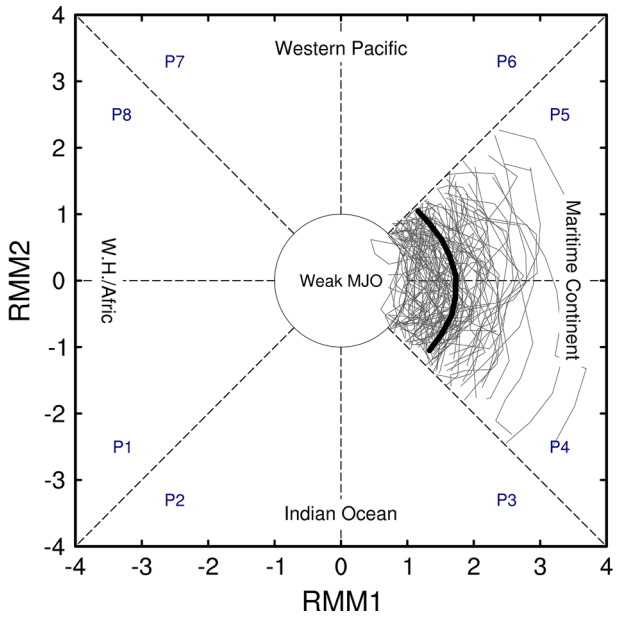

Fig. 1 | Propagation of MJO events across the Maritime Continent (MC). Phase-space trajectories of the 87 MJO events that successfully traversed the MC during 1981–2013. Thin gray lines denote individual event trajectories within phases 4 and 5, while the thick black line represents the composite trajectory.

when the event enters phase 4 from phase 3 (transitioning from the IO to the MC) and must remain ≥1.0 when exiting phase 5 (leaving the MC). Additionally, while traversing phases 4 and 5, the RMM amplitude must remain ≥1.0 for at least 65% of the days, and the trajectory must maintain a counterclockwise motion in phase space. These criteria are designed to maximize the sample size of valid MJO events, effectively filtering out those characterized by quasi-stationary behavior or distinct clockwise propagation within the phase diagram[41–43]. Based on these criteria, 87 MJO events were identified. Figure 1 illustrates the trajectories of these events as they traverse phases 4 and 5, revealing considerable diversity in amplitude and propagation speed.

The three systems mentioned above exhibit useful MJO prediction skill for about 16-21 days[44]. Additionally, our statistical analysis indicates that the average residence time of observed MJO events within phases 4 and 5 is approximately 10 days. Therefore, defining the time when the observed MJO enters phase 4 as "day 0", we selected forecast initialization times from 7 to 13 days prior to day 0 (denoted as day −13 to day −7). This time window was chosen to ensure that initialization is neither too close to day 0, which would likely result in all ensemble members successfully forecasting the MJO crossing the MC, nor too early, which might cause all members to fail to predict the crossing. This experimental design facilitates an effective assessment of the sensitivity of the MC-PB to initial uncertainty.

Due to differences in reforecast frequency among the three systems, the number of eligible ensemble forecast experiments varies for each observed MJO event. Specifically, the NCEP system (daily) provides up to 7 eligible initializations per event, whereas the BoM (six times per month) and ISAC systems (every five days) typically provide only 1–2. Consequently, for the 87 selected observed MJO events, the total number of eligible ensemble forecast experiments is 121 for BoM, 113 for ISAC, and 203 for NCEP (see Table 2).

Each forecast experiment comprises multiple ensemble members (see Table 1). Based on their ability to predict MJO propagation across the MC, these members are classified into two groups: those that successfully predict the crossing (MJO_C) and those that incorrectly forecast that the MJO is blocked by the MC (MJO_B). We further selected specific experiments from the set of eligible experiments (see Table 2) that contain both MJO_C and MJO_B members. Results indicate that such "mixed-member" experiments account for 69%, 44%, and 38% of the total eligible experiments in the BoM, ISAC, and NCEP systems, respectively. The BoM system exhibits the highest proportion, while the NCEP system shows the lowest. Figure 2a–c show the predicted RMM indices for MJO_C and MJO_B members in each system. Before entering the MC, the propagation trajectories predicted by MJO_C and MJO_B members are nearly identical. However, after entering the MC, although the MJO amplitude predicted by MJO_C decays slightly, it maintains sufficient intensity to continue eastward propagation and eventually crosses the MC. In contrast, the MJO amplitude predicted by MJO_B weakens rapidly, resulting in a failure to cross the MC.

Table 2 | Number of selected ensemble forecast experiments

Model	Experiments meeting initialization criteria	Experiments with mixed members
BoM	121	83
ISAC	113	50
NCEP	203	78

We quantified the forecast skill for these two categories using the ACC between the observed and predicted RMM indices, as defined in Eq. (3).

$$ACC(\tau)=\frac{\sum_{t=1}^{t=N}[a_1(t)b_1(t,\tau)+a_2(t)b_2(t,\tau)]}{\sqrt{\sum_{t=1}^{t=N}[a_1^2(t)+a_2^2(t)]}\sqrt{\sum_{t=1}^{t=N}[b_1^2(t,\tau)+b_2^2(t,\tau)]}} \quad (3)$$

$(a_1(t), a_2(t))$ are the observed RMM indices at time t. $(b_1(t,\tau), b_2(t,\tau))$ are the corresponding forecasts at lead τ days. The total number of forecast experiments is represented by N. Figure 2d–f present the ensemble-mean forecast skill for the two groups of members in the three systems. The figures show that when the forecast lead time is less than 10 days, the prediction skill of both groups is comparable. However, beyond 10 days, the skill of MJO_B members drops rapidly, whereas the skill of MJO_C members declines much more gradually. Using the standard threshold of 0.5 for skillful prediction, the difference in effective forecast lead time between the two groups exceeds 6 days, reaching over 16 days in the BoM and NCEP systems.

Crucially, for a given ensemble forecast experiment from the same system, MJO_C and MJO_B members share the same model physics and initialization time. Therefore, the divergence in their forecast performance can be attributed exclusively to differences in their initial conditions. Moreover, as shown above, these members exhibit distinct propagation characteristics across the MC. These results confirm that initial uncertainty can significantly impact both the MJO propagation behavior over the MC and its forecast skill. The pronounced contrast between MJO_C and MJO_B suggests that initial errors alone can lead to the MC-PB. This finding raises a critical question: which specific spatial pattern of initial error is more likely to trigger the MC-PB and produce the largest forecast errors? Addressing this question is crucial for determining whether improving initial conditions can alleviate the MC-PB effect and improve MJO forecast skill.

Initial errors prone to triggering the MC-PB

The occurrence of the MC-PB tends to result in substantially larger MJO forecast errors. Therefore, to reveal the specific initial error patterns that are more prone to trigger the MC-PB, we first examine the initial error that produces the largest MJO forecast deviations. As detailed in Methods, the CNOP method is designed to determine the initial error that yields the maximum forecast errors. Accordingly, this section employs the CNOP method to identify the initial errors prone to triggering the MC-PB, thereby providing new insights for reducing MJO forecast errors and improving prediction skill.

To determine which physical variable's initial uncertainty exerts the greatest influence on MJO prediction, we first assess the sensitivity of MJO forecasts to initial uncertainties in key atmospheric variables. Wei et al.[45] found that initial moisture perturbations can trigger the onset of MJO events, while Wu et al.[46] and Zeng et al.[47] demonstrated that improvements

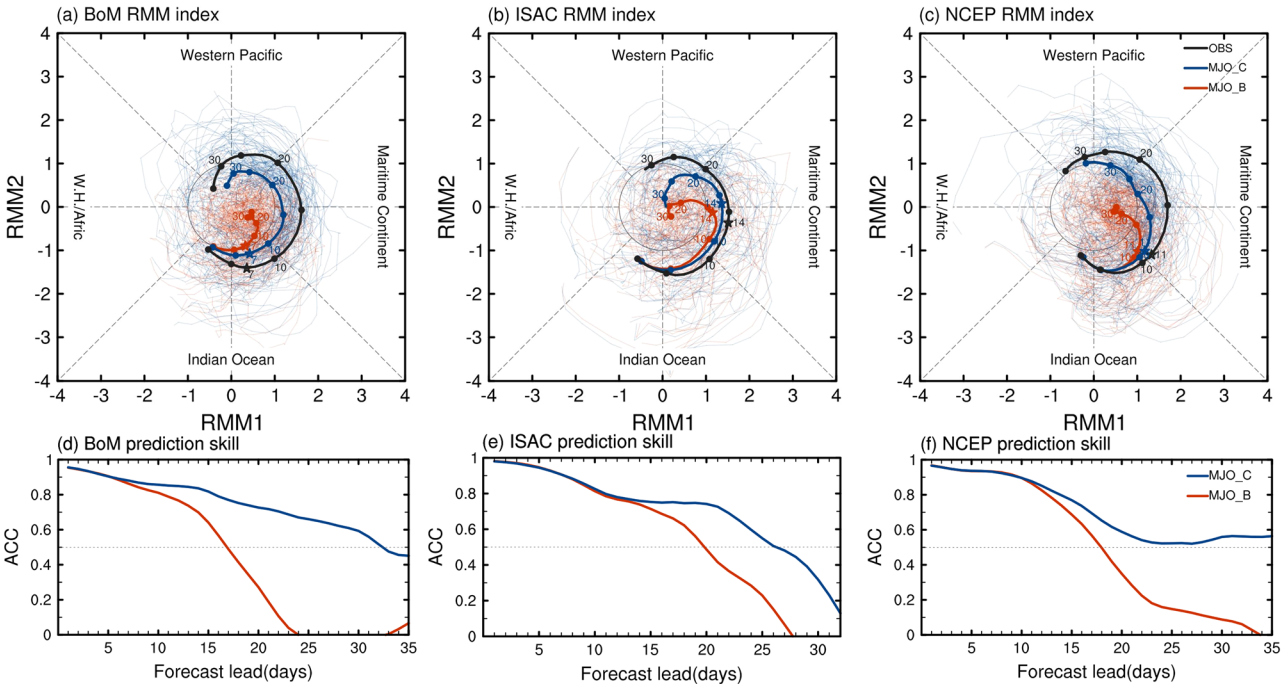

Fig. 2 | Comparison of MJO prediction performance between MJO_C and MJO_B members in three S2S forecast systems. Panels (a–c) show RMM phase-space trajectories, and panels (**d–f**) display bivariate anomaly correlation coefficients (ACC) as a function of forecast lead time, with columns from left to right corresponding to the BoM, ISAC, and NCEP systems, respectively. Blue and red lines represent the MJO_C and MJO_B categories, respectively. In (**a–c**), thin lines denote ensemble means of individual forecast experiments, thick colored lines indicate the composite mean for each category, and the thick black line represents the observational composite. Small dots along each trajectory indicate 5-day intervals. The asterisk indicates the onset of statistically significant differences between the two categories (95% confidence level, $p < 0.05$).

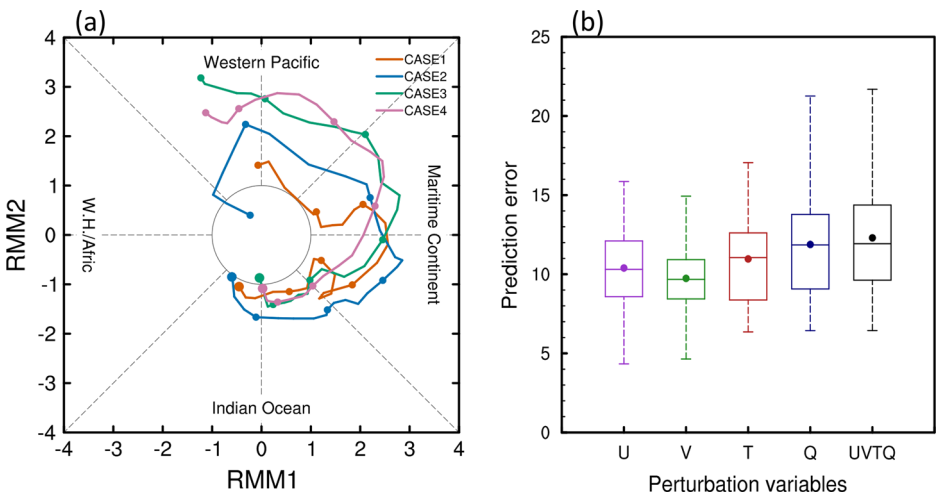

Fig. 3 | MJO events and forecast error sensitivity to initial perturbations. a Phase-space trajectories of the RMM index of four propagating MJO events from CESM1 free-running simulation. Markers along each trajectory indicate 5-day intervals, with larger symbols denoting initialization times. **b** Boxplots of MJO forecast errors induced by initial perturbations in zonal wind (U), meridional wind (V), temperature (T), specific humidity (Q), and their combination (UVTQ). Solid dots denote the mean forecast error.

in moisture initialization schemes effectively enhance MJO forecast skill. Meanwhile, Bengtsson et al.[31] suggested that initial temperature errors may affect forecast skill by modulating atmospheric static stability. Given that moisture advection is a key mechanism for the eastward propagation of the MJO[48,49], initial wind errors may also play a critical role. These considerations raise an important question: which physical variable's initial uncertainty has the most significant impact on MJO forecasts?

To address this question, we selected four propagating MJO events from long-term free-running simulations of CESM1 (see Fig. 3a). For each event, perturbations were individually superimposed on the initial conditions of zonal wind (U), meridional wind (V), temperature (T), and specific humidity (Q) to examine the sensitivity of MJO forecast errors to initial uncertainties in these variables. Among the three ensemble forecast systems used in the S2S hindcast statistics, only the NCEP system provides publicly available initial perturbations. Therefore, we randomly sampled 30 sets of initial perturbations from the NCEP system and added the corresponding components to the initial conditions for the four MJO events. Considering that the tropical IO is the primary initiation and active region for the MJO, perturbations were confined to this domain (15°S–15°N, 40°E–110°E, 1000–500 hPa, corresponding to the lowest 12 levels in the CAM). The MJO forecast errors caused by initial perturbations are quantified as follows:

$$J = \sum_{n=1}^{N} \sqrt{\left[RMM_1^{Pert}(t_n) - RMM_1^{Ctrl}(t_n)\right]^2 + \left[RMM_2^{Pert}(t_n) - RMM_2^{Ctrl}(t_n)\right]^2} \quad (4)$$

where the superscripts "*Ctrl*" and "*Pert*" represent the control experiment (without initial perturbation) and the perturbation experiment (with initial perturbation), respectively. N represents the forecast length of 25 days.

Figure 3b shows boxplots of the MJO forecast errors resulting from initial perturbations in different variables. It is evident that the sensitivity of MJO forecasts to initial uncertainties varies markedly among variables. Compared with other variables, perturbations in specific humidity (Q) yield a much wider error spread and a larger mean forecast error. Notably, the uncertainty range and mean error driven by Q perturbations alone are comparable to those induced by the combined perturbations in U, V, T, and Q. These results indicate that, among the variables considered, MJO forecasts are most sensitive to initial moisture perturbations. Consequently, subsequent analyses focus on the moisture field to characterize the initial errors that exert the most profound influence on MJO forecasting.

We selected the tropical IO (15°S–15°N, 40°E–110°E, 1000–500 hPa, corresponding to the lowest 12 levels in the CAM) as the perturbation domain. Inequality (5) was adopted as the constraint to limit the amplitude of the initial error for calculating the CNOP-type initial moisture error, which is defined as:

$$||q'|| = \sqrt{\sum_{i,j,k}(q'_{i,j,k})^2/M} \le \delta \tag{5}$$

where $q'_{i,j,k}$ represents the initial specific humidity error at the perturbed grid point (i, j, k), and M denotes the total number of grid points within the perturbation domain. Based on the magnitude of analysis errors for specific humidity in the tropics[50], the constraint parameter δ is set to 0.0005 kg/kg. The objective function, given by Eq. (4), measures the accumulated MJO forecast error over a 25-day forecast period. Under this optimization framework, the CNOP-type initial moisture error is defined as the constrained initial perturbation that maximizes the cumulative forecast error of the RMM index.

We calculated the CNOP-type initial moisture error for each of the four MJO events (see Fig. 4). For CASE1 and CASE2, the initial errors exhibit similar spatial structures, characterized by a distinct zonal dipole pattern in the horizontal and a baroclinic structure in the vertical. Specifically, in the lower troposphere, the western Indian Ocean (WIO) exhibits predominantly positive moisture errors, which gradually transition to negative errors with height. Conversely, the eastern Indian Ocean (EIO) exhibits strong negative moisture errors in the lower levels, which transition to positive errors in the upper levels. The error structures for CASE3 and CASE4 also display similarities in the mid-troposphere (approximately model levels k = 19–21), featuring positive errors over the southwestern IO, negative errors over the northern central-eastern IO, and weak positive errors over western Indonesia. Further analysis of the low-level structures reveals that CASE3 features a northwest–southeast oriented band of alternating positive and negative errors, although the error magnitude is notably smaller. For CASE4, the lower troposphere over the WIO and EIO is dominated by negative moisture errors, while the central IO features weak positive errors.

Figure 5 illustrates the evolution of MJO events in the CNOP experiments, which were obtained by superimposing CNOP-type errors on the initial conditions of the CTRL experiments (the unperturbed control runs). As shown in the figure, the impact of CNOP-type initial errors on the MJO exhibits distinct case dependence. In CASE1 and CASE2, the predicted MJO propagation speed is significantly reduced after entering the MC, leading to stagnation (CASE2; see Fig. 5b) or even retrogradation (CASE1; see Fig. 5a). Consequently, the final phases lag behind the CTRL experiments by nearly two phases (see Figs. 5i, j). In CASE3 and CASE4, the predicted MJO weakens rapidly after entering the MC, with a maximum decay rate of 0.4 day^{-1}, corresponding to a reduction of approximately 15% of the MJO amplitude relative to the CTRL experiment (see Figs. 5g, h).

To verify that the CNOP represents the optimal error yielding the largest MJO forecast errors, we conducted two supplementary experiments. First, for each MJO event, we superimposed 30 sets of spatially random errors on the initial conditions of the CTRL experiment (denoted as the "RAND" experiment). We rescaled these errors so that their magnitudes are comparable to those of the CNOP-type errors. The MJO propagation trajectories in the RAND experiments remain largely consistent with the CTRL experiments, with negligible amplitude and phase forecast errors. This suggests that, compared with the CNOP-type errors, which possess coherent spatial structures, the impact of unstructured random noise on MJO forecast uncertainty is negligible.

Second, we compared the CNOP-type initial errors with realistic initial errors. Since only the NCEP system provides publicly available initial perturbation data, we randomly sampled 30 sets of initial specific humidity errors from the NCEP ensemble forecast system. These errors were rescaled to match the magnitude of the CNOP-type errors and then superimposed on the initial condition of the CTRL experiment (denoted as the "NCEP" experiment). As shown in Fig. 5, the NCEP errors induce substantially larger forecast deviations than RAND, resulting in greater mean amplitude and phase errors, as well as a wider spread of forecast errors. However, these deviations remain considerably smaller than those induced by CNOP-type errors. This indicates that structured NCEP errors yield greater forecast uncertainty than random noise, yet still lead to smaller forecast errors than CNOP-type errors.

Figure 6 displays the spatial patterns of initial moisture errors yielding the maximum forecast errors among the 30 selected NCEP samples for each case. These errors exhibit spatial similarities to the CNOP-type errors in certain regions. For instance, in CASE1 and CASE2, both error types feature negative perturbations in the lower levels of the EIO (k = 28–30) and the upper levels of the WIO (k = 19–21). Similarly, in CASE3 and CASE4, both errors display negative perturbations in the upper levels over the northern central IO (k = 19–20) and local positive perturbations in the middle levels over the northern WIO (k = 22–26). Nevertheless, a key distinction remains: the CNOP-type errors possess a significantly more coherent and concentrated spatial structure. This structural difference likely explains why the CNOP-type errors are more effective at inducing large forecast deviations. These findings naturally raise the next question: do these CNOP-type errors represent the initial errors more likely to induce the MC-PB?

Figure 7 illustrates the daily evolution of forecast errors and their growth rates caused by the CNOP-type errors and the specific NCEP errors shown in Fig. 6. The daily forecast error [denoted as $E(t_n)$] and its growth rate [denoted as $R(t_n)$] are defined as:

$$\mathrm{E}(t_n) = \sqrt{[\mathrm{RMM}_1^{Pert}(t_n) - \mathrm{RMM}_1^{Ctrl}(t_n)]^2 + [\mathrm{RMM}_2^{Pert}(t_n) - \mathrm{RMM}_1^{Ctrl}(t_n)]^2} \tag{6}$$

$$\mathrm{R}(t_n) = \frac{\mathrm{E}(t_n) - \mathrm{E}(t_{n-1})}{t_n - t_{n-1}}, \tag{7}$$

As shown in Fig. 7, forecast errors associated with both types of initial errors increase with forecast lead time, with the error growth accelerating notably after the MJO enters the MC. Furthermore, the CNOP-type errors exhibit higher growth rates than the NCEP errors. This evidence confirms that the CNOP-type errors, characterized by their specific spatial structure, are particularly prone to generating substantial MJO forecast errors and inducing the MC-PB. This leads to a critical follow-up question: through what physical mechanisms do these CNOP-type errors generate such substantial MJO forecast errors and lead to the MC-PB? This issue will be addressed in the next section.

Mechanisms by which CNOP-type errors trigger significant MC-PB

The results presented above indicate that the causes of the MC-PB induced by CNOP-type initial errors are case-dependent. Specifically, in CASE1 and CASE2, the MC-PB manifests primarily as a significant slowdown in MJO propagation over the MC. Conversely, in CASE3 and CASE4, it stems

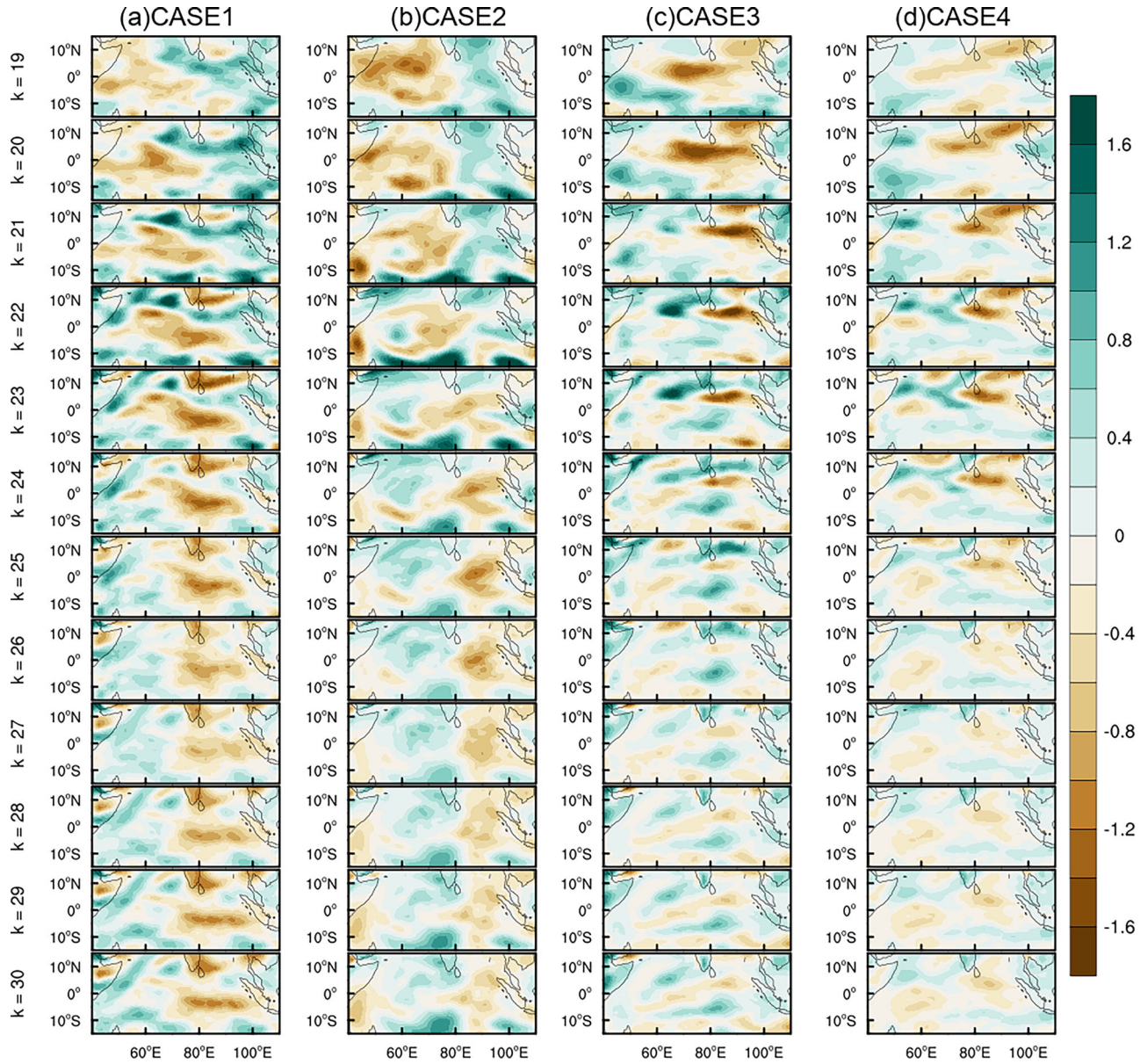

Fig. 4 | Spatial structures of the CNOP-type initial moisture errors. Panels (**a**–**d**) show the specific humidity errors (g kg^{-1}) for CASE1–CASE4, from left to right. Each row represents a different model level, from the upper troposphere (top) to the lower troposphere (bottom).

largely from the sharp weakening of MJO intensity after entering the MC. Therefore, in this section, we select CASE1 and CASE3 as representative cases to elucidate the specific physical mechanisms through which the CNOP-type initial errors trigger a significant MC-PB.

We first investigate the physical mechanisms driving the MJO phase lag in CASE1. Intraseasonal anomalies were extracted using a 20–100-day Lanczos bandpass filter[51] with 201 weights. Figure 8 illustrates the spatio-temporal evolution of OLR and 850-hPa wind anomalies for the CTRL and CNOP experiments in CASE1. As shown in Fig. 8a, in the CTRL experiment, active convection is initially centered over the WIO, accompanied by low-level westerly anomalies to its west and strong easterly anomalies to its east. Subsequently, this active convection propagates steadily eastward, passing through the EIO and entering the MC. However, under the influence of the CNOP-type error, the differences between the CNOP and CTRL experiments become increasingly pronounced from forecast day 15 onwards (see Fig. 8b, c). In contrast to the CTRL experiment, where active convection continues to develop over the MC and propagates slowly eastward, the active convection in the CNOP experiment reverses direction, propagating westward back to the WIO, accompanied by a distinct equatorially symmetric cyclonic circulation. Concurrently, suppressed convection emerges over the WP, straddling the equator. This suppressed convection propagates westward synchronously with the active convection over the IO, reaching the MC by day 25. In summary, the CNOP-type error fundamentally alters the coupled evolution of large-scale convection and circulation, shifting the coupled system from an eastward-propagating mode to a westward-propagating mode. This transition results in a distinct prediction barrier as the MJO traverses the MC.

The comparison above indicates that the primary distinction between the CNOP and CTRL experiments is the emergence of a robust westward-propagating disturbance in the former. A critical question arises: What is the physical origin of this westward-propagating disturbance? DeMott et al.[52] noted that a westward-propagating "transient dry precursor (TDP)" is present in roughly half of MJO events as they traverse the MC. The TDP is identified as the dry phase of an equatorial Rossby (ER) wave, which can impede MJO eastward propagation by eroding MJO moisture anomalies. Similarly, Wei et al.[53] reported that westward-propagating ER waves can influence MJO eastward propagation, leading to diverse propagation characteristics. Motivated by these studies, we hypothesize that the

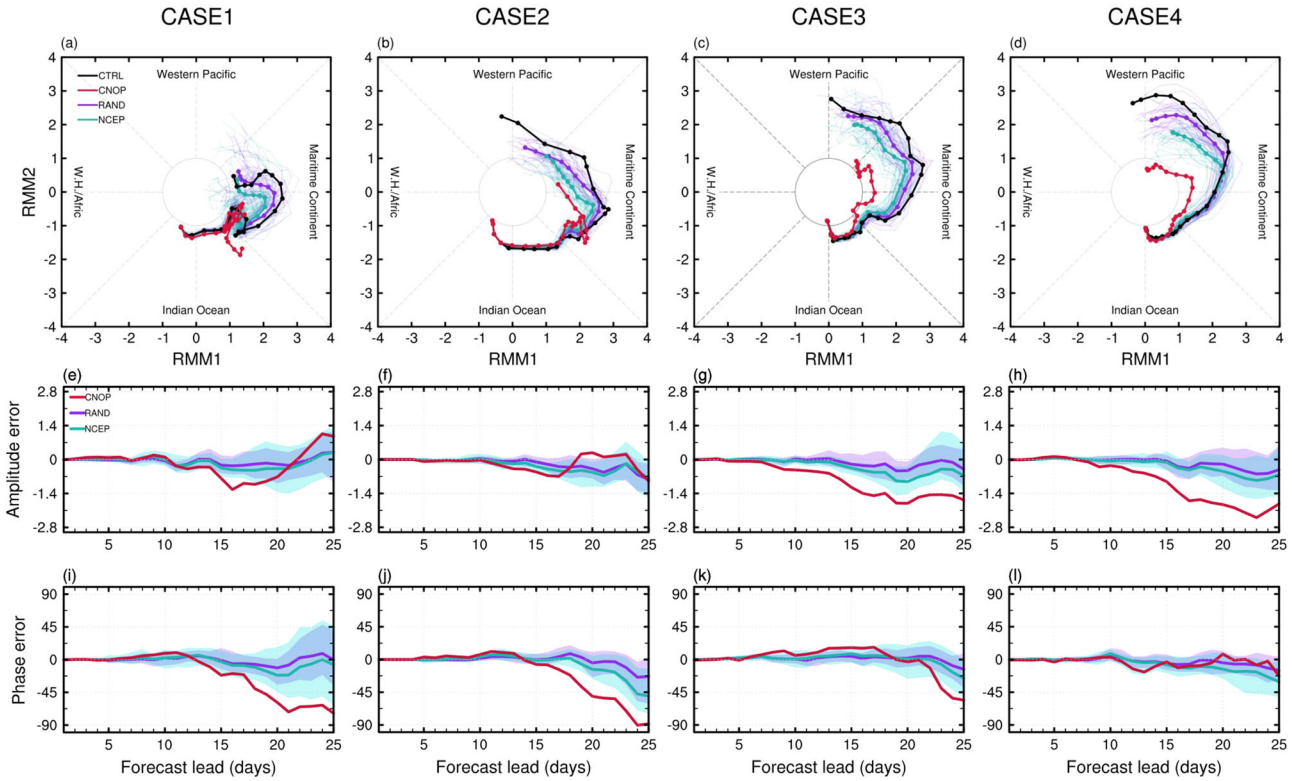

Fig. 5 | Evolution of RMM indices and forecast errors in different perturbation experiments. The top row (**a**–**d**) shows the phase-space diagrams, the middle row (e–h) shows the amplitude errors, and the bottom row (**i**–**l**) shows the phase errors, for CASE1–CASE4 from left to right. Black, red, purple, and cyan lines denote CTRL, CNOP, RAND, and NCEP experiments, respectively. For the RAND and NCEP experiments, thin lines represent individual perturbation samples, while thick lines represent the average of all samples.

westward-propagating disturbance observed in the CNOP experiment is closely related to ER wave activity. To test this, we applied the wavenumber-frequency filtering method[54] to isolate the ER wave component from the OLR anomalies. This approach enables us to diagnose whether the CNOP-type error inhibits MJO eastward propagation by modulating westward-propagating ER waves.

Figure 9a presents the Hovmöller diagram of the MJO and ER wave components. In the CTRL experiment, an eastward-propagating negative OLR anomaly is clearly evident. This anomaly, primarily attributed to MJO active convection, reaches the MC around forecast day 15 and maintains its development in this region for the subsequent 10 days. Notably, a westward-propagating ER wave from the central Pacific exhibits a "wet-leading-dry" phase structure and naturally dissipates near 120°E. In contrast, in the CNOP experiment, the MJO-related negative OLR anomaly remains confined to the IO. Crucially, both the wet and dry phases of the ER wave are significantly amplified. The wet phase propagates westward into the WIO, while the dry phase propagates westward into the MC. Since the amplified ER wave becomes stronger than the MJO signal, the MJO suppressed-convection signature over the WIO is replaced by the ER wet phase, while the ER dry phase suppresses the MJO active convection across the MC.

In summary, for CASE1, the CNOP-type error primarily amplifies the intensity of the westward-propagating ER wave. This amplified ER wave dominates the evolution of tropical intraseasonal convection and circulation signals, thereby suppressing MJO eastward propagation and ultimately leading to a pronounced prediction barrier over the MC.

We now investigate the physical processes associated with the weakened MJO intensity in CASE3. Figure 10 presents the spatio-temporal evolution of OLR and 850-hPa wind anomalies for the CTRL and CNOP experiments in CASE3. As shown in Fig. 10a, in the CTRL experiment, active convection is initially centered over the central IO, while the MC is dominated by suppressed convection accompanied by strong low-level easterly anomalies. By forecast day 10, active convection begins to develop over the MC. Subsequently, the convective center shifts southward, detouring through the southern MC before re-establishing over the WP. This propagation pathway is consistent with the observed "detour" characteristic of the boreal winter MJO[48]. During this process, the active convection is flanked by low-level easterly anomalies to its east (reflecting the Kelvin wave response) and low-level westerly anomalies to its west (dominated by the twin cyclonic gyres characteristic of the ER wave). These wind anomalies are tightly coupled with the convection, forming a coherent convection-circulation system that propagates slowly eastward. However, in the CNOP experiment, while the propagation trajectory remains largely consistent with the CTRL experiment, the intensity of the system is markedly weakened (see Fig. 10b). As evidenced in Fig. 10c, these differences in intensity become pronounced as early as day 10, when the active convection is still located over the EIO. This attenuation intensifies as the MJO propagates eastward. In summary, in CASE3, while the CNOP-type error does not alter the MJO propagation pathway, it significantly dampens the intensity of the entire coupled convection-circulation system during its passage over the MC, thereby inducing the MC-PB.

Figure 9b illustrates the propagation characteristics of the MJO and ER wave components in CASE3, following the analysis of CASE1. As seen in Fig. 9b, in the CTRL experiment, MJO active convection initiates over the central IO, successfully traverses the MC, and enters the WP. Conversely, in the CNOP experiment, despite following the same trajectory, the MJO active convection is severely weakened, particularly over 110°–140°E, where convective activity becomes negligible. Analysis of the ER wave reveals that in the CTRL experiment, the ER wave energy disperses eastward. However, the superimposed CNOP-type error modifies the structure and intensity of this wave train, generating an eastward-dispersing disturbance wave train dominated by dry perturbations. This indicates that the suppressive effect of this disturbance wave train on MJO active convection outweighs the

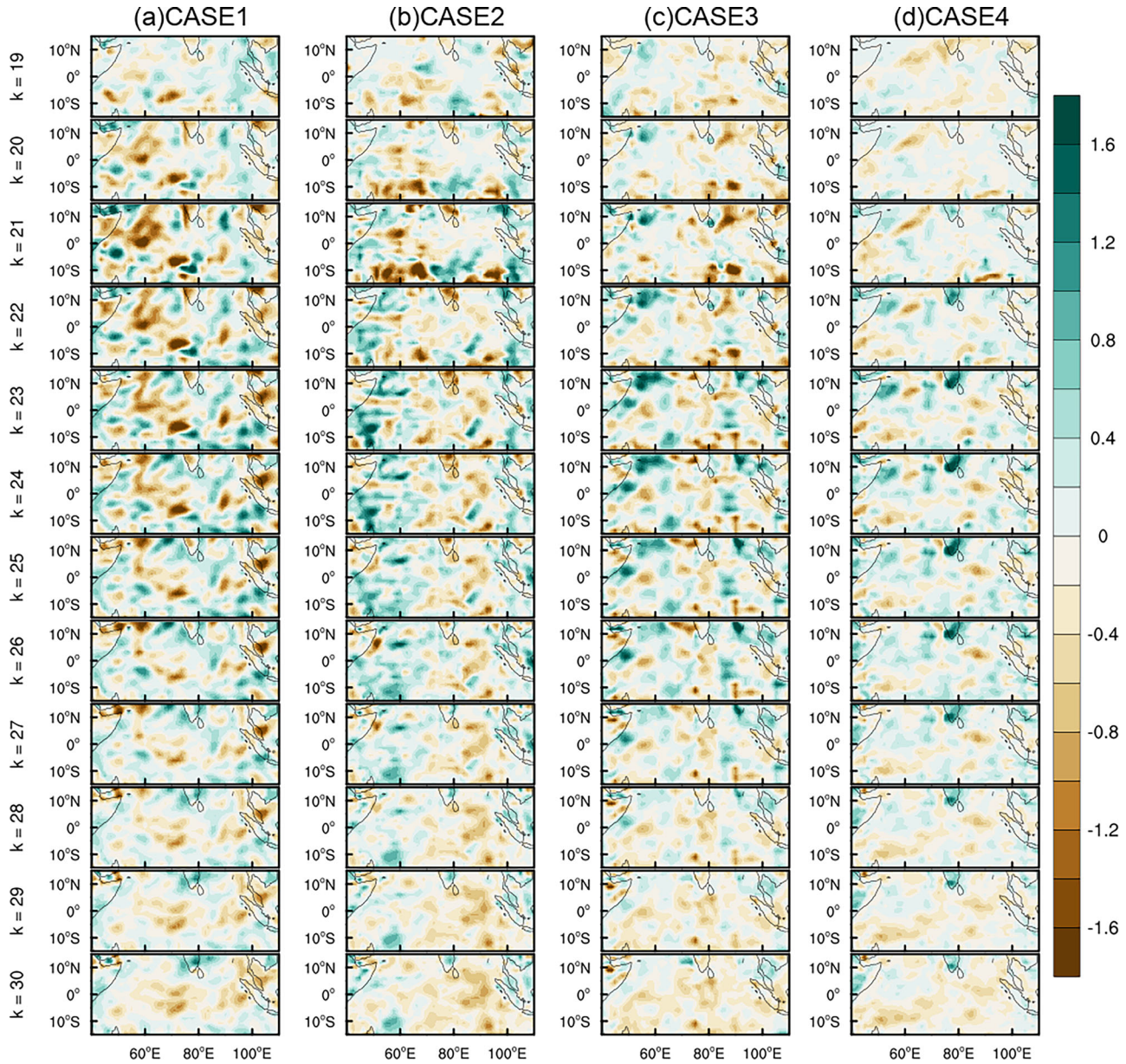

Fig. 6 | Spatial structures of the NCEP initial moisture errors. Same as Fig. 4, but for the NCEP initial specific humidity errors yielding the maximum forecast errors among the 30 perturbation samples for (**a**) CASE1, (**b**) CASE2, (**c**) CASE3, and (**d**) CASE4.

constructive effect. Specifically, during forecast days 15–20, the ER wave dry disturbance between 110°E and 140°E effectively erodes the intensity of the MJO active convection. Therefore, for CASE3, the CNOP-type error also impacts MJO propagation by modulating the westward-propagating ER wave. However, the distinction between CASE3 and CASE1 lies in the manifestation of this impact: in CASE3, the error primarily alters the local wave train structure to weaken MJO intensity, whereas in CASE1, it primarily amplifies the large-scale westward-propagating ER wave, thereby altering the MJO propagation direction.

As indicated by the above discussion, by forecast day 10, when the MJO active convection is located over the EIO, the convection intensity in the CNOP experiment is already significantly weaker than in the CTRL experiment. Barrett et al.[55] noted that "active" MJO events exhibit stronger amplitudes as early as three days prior to entering the MC compared to "weakening" events. Accordingly, we hypothesize that under similar background states, the MJO intensity prior to entering the MC may be a critical factor determining whether it can traverse the MC with robust intensity. To this end, we investigate how the attenuation of MJO intensity over the EIO contributes to its subsequent decay over the MC. The moisture budget is evaluated following the diagnostic approach of Yanai et al.[56] using Eq. (8).

$$\frac{\partial q}{\partial t} = -V_h \cdot \nabla_h q - \omega \cdot \frac{\partial q}{\partial p} - \frac{Q_2}{L_v}, \tag{8}$$

where $V_h = (u, v)$ represents the horizontal wind vector, $\nabla_h = (\partial/\partial x, \partial/\partial y)^T$ denotes the horizontal gradient operator, ω represents the vertical pressure velocity, p is the pressure, q denotes the specific humidity, and t is the time, Additionally, Q_2 and L_v represent the atmospheric apparent moisture sink and the latent heat of condensation, respectively. The right-hand-side terms account for horizontal moisture advection, vertical moisture advection, and moisture sink, respectively. The moisture sink is diagnosed as the residual between the moisture tendency and the combined advection components[56–58].

Figure 11 displays longitude-height sections of the intraseasonal moisture and wind anomalies averaged over the equatorial region (20°S–10°N) and over forecast pentad 2 (days 6–10) and pentad 3

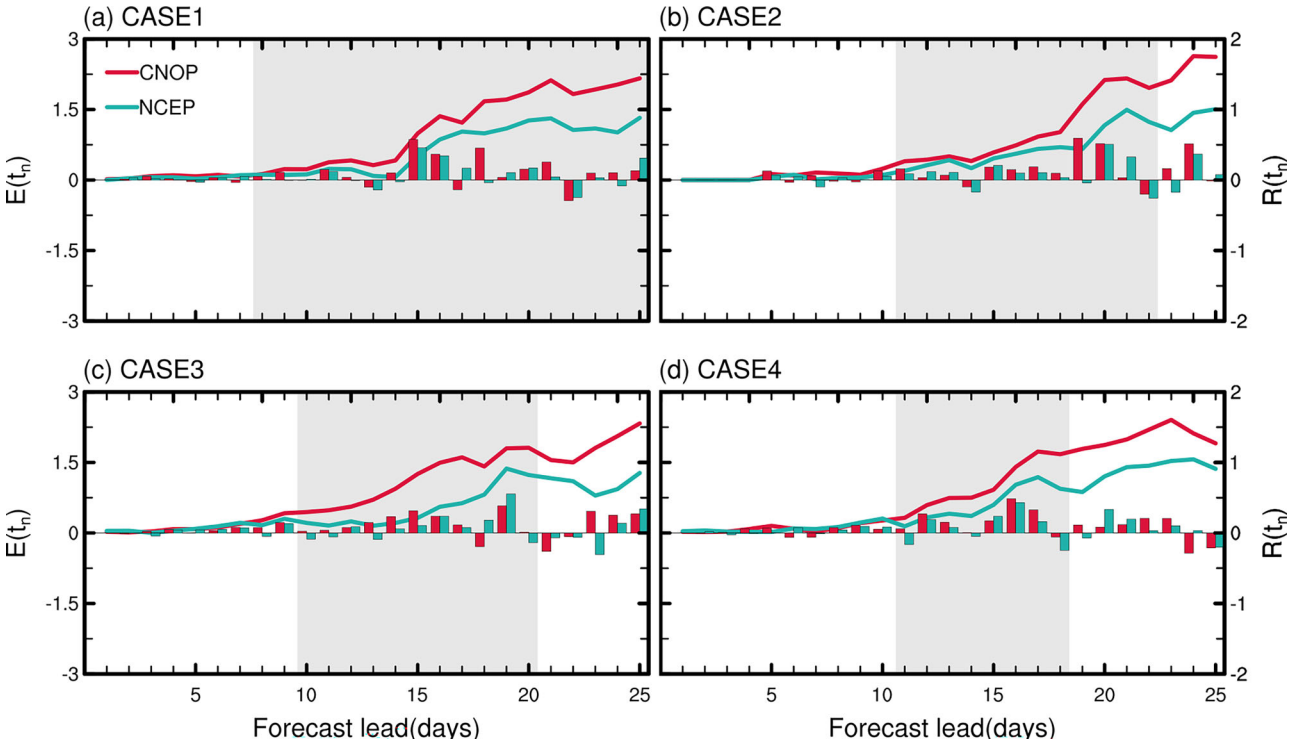

Fig. 7 | Daily evolution and growth rates of MJO forecast errors induced by CNOP and NCEP initial errors. Lines show the daily evolution of MJO forecast errors, and bars represent their growth rates, from the CNOP-type initial errors and the specific NCEP initial errors shown in Fig. 6. The shaded region denotes the period when the MJO propagates through phases 4-5 in the CTRL experiment. Panels (**a**–**d**) show the results for CASE1–CASE4, respectively.

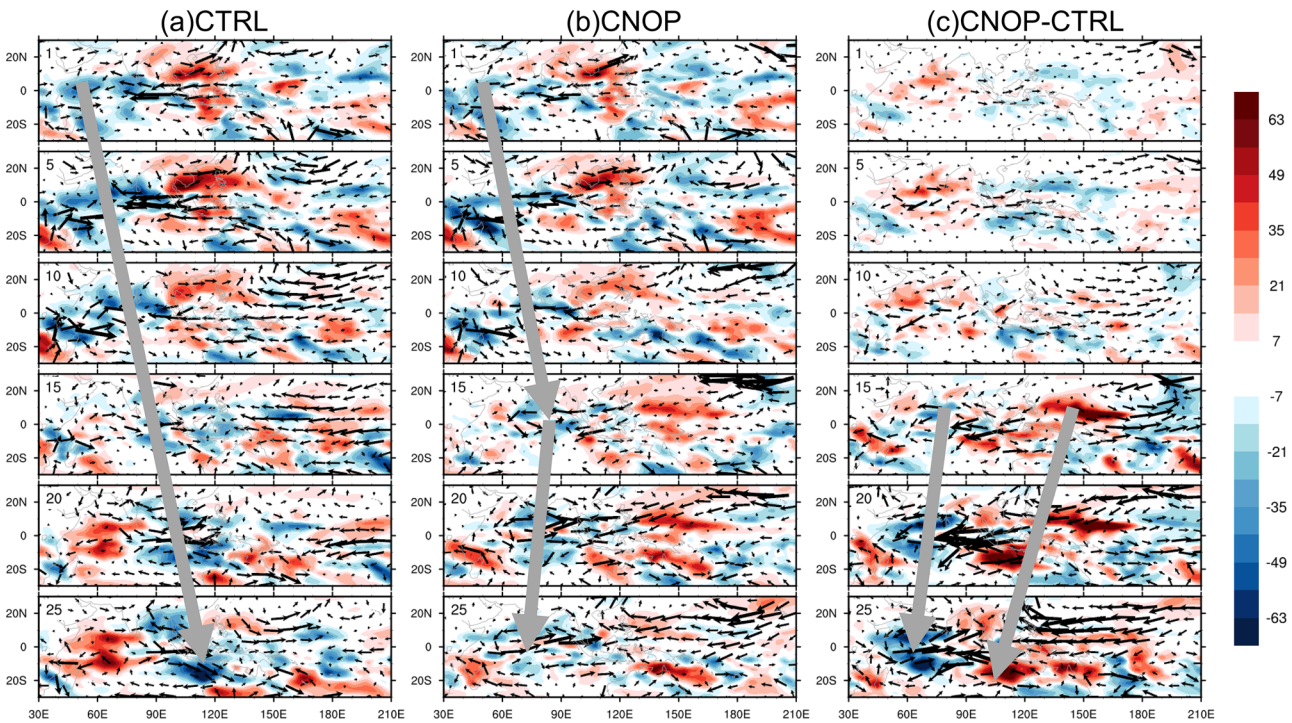

Fig. 8 | Evolution of anomalous OLR and 850-hPa wind. Spatio-temporal evolution of OLR anomalies (shading; units: W m^{-2}) and 850-hPa wind anomalies (vectors; units: m s^{-1}). Panels (**a**–**c**) show the CTRL experiment, the CNOP experiment, and their difference (CNOP minus CTRL), respectively.

(days 11–15). As shown in Fig. 11a, during pentad 2 of the CTRL experiment, the active convection center is located over the EIO, accompanied by strong ascending motion and deep positive moisture anomalies. Conversely, the WP is dominated by suppressed convection, characterized by descending motion and dry anomalies. Over the MC, a circulation system comprising low-level easterly and upper-level westerly anomalies is evident. This circulation system, termed the "front Walker cell" (FWC)[59], is considered important for MJO eastward propagation. Specifically, the low-level

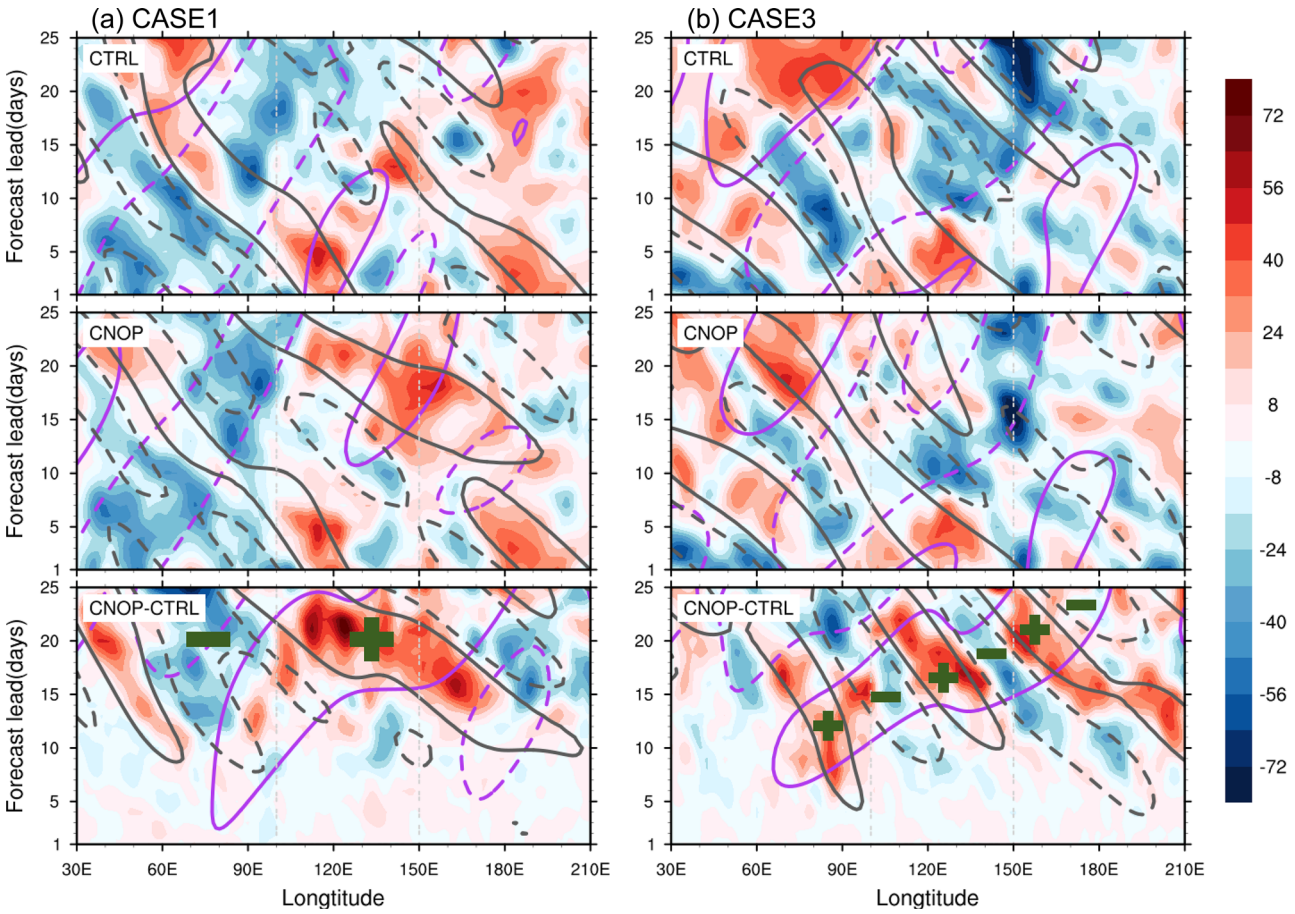

Fig. 9 | Time-longitude evolution of equatorial OLR anomalies and wave components. Hovmöller diagrams of OLR anomalies (shading; units: W m^{-2}) averaged over 20°S–10°N for (**a**) CASE1 and (**b**) CASE3. Purple and black contours denote MJO and ER wave components, respectively, plotted at ± 10 W m^{-2}. Solid (dashed) lines indicate positive (negative) anomalies.

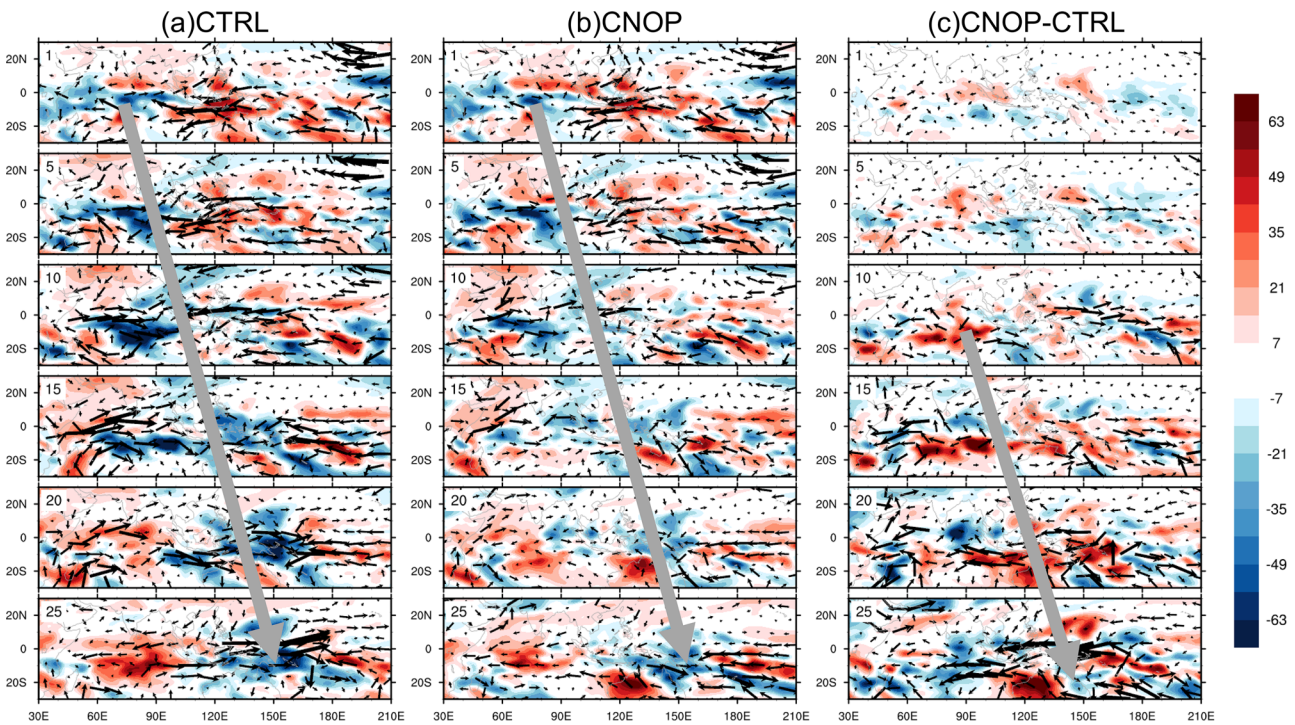

Fig. 10 | Evolution of anomalous OLR and 850-hPa wind. Same as Fig. 8, but for CASE3. Panels (**a**–**c**) show the CTRL experiment, the CNOP experiment, and their difference (CNOP minus CTRL), respectively.

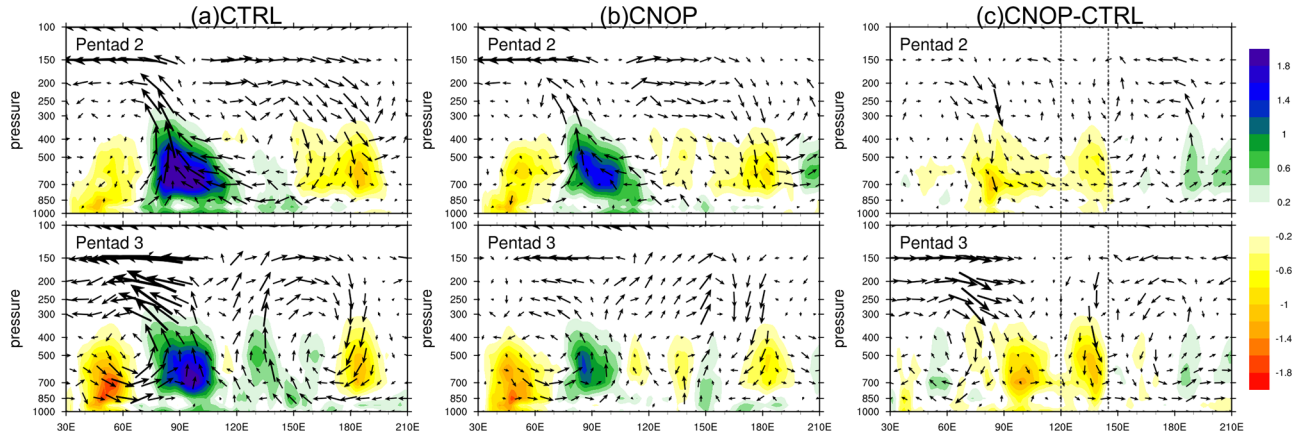

Fig. 11 | Impacts of CNOP-type initial errors on the vertical structures of intraseasonal moisture and wind anomalies. Longitude-height sections of intraseasonal specific humidity anomalies (shading; units: g kg^{-1}) and wind anomalies (vectors; units: m s^{-1} averaged over 20°S–10°N during pentad 2 and pentad 3. Panels (**a**–**c**) show the CTRL experiment, the CNOP experiment, and their difference (CNOP minus CTRL), respectively.

Fig. 12 | Impact of CNOP-type initial errors on the vertical structure of the moisture budget over the MC. Vertical profiles of moisture budget terms (units: g kg^{-1} day^{-1}) averaged over the MC region (20°S–10°N, 120°E–145°E) for (**a**) pentad 2 and (**b**) pentad 3. Solid and dashed lines denote the CTRL and CNOP experiments, respectively.

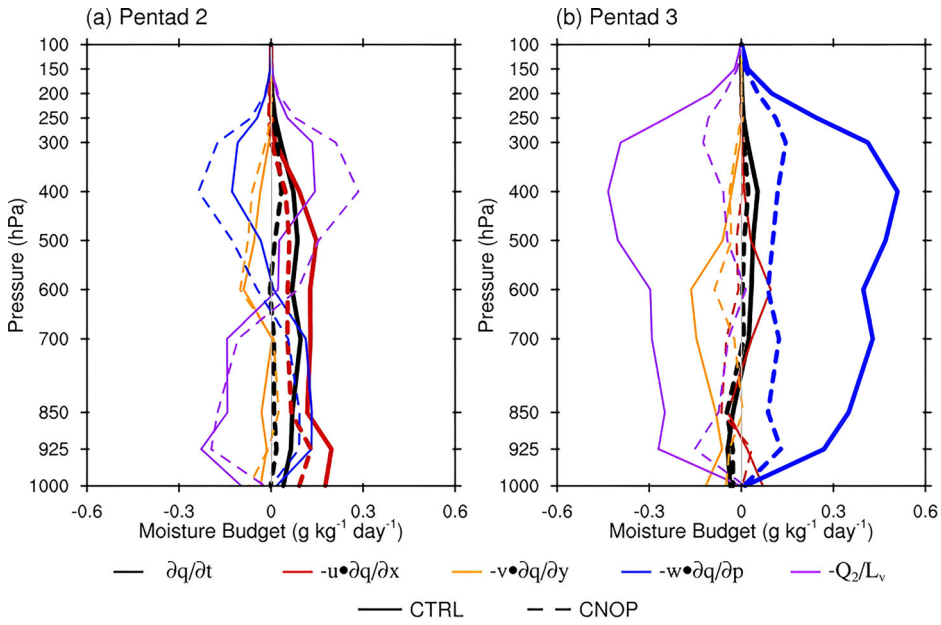

easterlies enhance boundary layer moisture convergence, facilitating atmospheric pre-moistening and creating favorable conditions for the initiation of congestus convection. However, after superimposing the CNOP-type initial error, the intensity of the active convection and ascending motion over the EIO is significantly weakened (see Figs. 10c and 11). Consequently, due to the reduced diabatic heating, the easterly anomalies associated with the low-level Kelvin wave response over the MC are substantially attenuated. This attenuation diminishes boundary layer moisture and weakens the critical atmospheric pre-moistening process, consequently suppressing the initiation and development of new convection to the east of the primary convection center. By forecast pentad 3, in the CTRL experiment, strong ascending motion and positive moisture anomalies are established over the MC, facilitating the vertical transport of low-level moisture to the mid-to-upper troposphere and promoting moistening at these levels. This process facilitates the evolution from congestus to deep convection, shifting the convective center eastward from the EIO toward the MC. In contrast, in the CNOP experiment, the ascending motion and positive moisture anomalies over the MC are markedly weakened or even absent, with only faint signals remaining near 150°E. The weakened ascent impedes the vertical transport of moisture, resulting in insufficient moistening in the mid-to-upper troposphere and preventing the establishment of deep convection over the MC. These results suggest that the CNOP-type error dampens the main MJO convection over the EIO, thereby weakening the downstream easterly Kelvin wave response. The reduced pre-moistening over the MC inhibits local convection growth, which eventually causes the MJO to weaken significantly as it traverses the MC.

To elucidate the physical processes governing the moisture reduction over the MC, Fig. 12 presents vertical profiles of moisture budget terms averaged over the MC (20°S–10°N, 120°E–145°E). During pentad 2, the CTRL experiment exhibits a vertically coherent moistening tendency throughout the tropospheric column. Specifically, the zonal advection acts as the primary positive contributor to moistening across the entire column, whereas the meridional advection induces drying. The vertical advection contributes to moistening in the lower troposphere but acts as a drying term in the mid-to-upper troposphere. The moisture sink exhibits an opposite vertical distribution, which largely offsets the vertical advection. In contrast, the reduction in the moisture tendency in the CNOP experiment is primarily attributed to the decrease in zonal moisture advection, with a secondary contribution from the vertical advection. By pentad 3, while the

boundary layer begins to dry in the CTRL experiment, the mid-to-upper troposphere maintains a moistening trend, driven primarily by the vertical advection. Conversely, the negligible tropospheric moistening in the CNOP experiment is attributed to the collapse of the vertical advection, which inhibits the effective upward transport of moisture.

In summary, the CNOP-type error in CASE3 acts to weaken the active convection over the EIO, which in turn attenuates the Kelvin wave response driven by this deep convective heating. The weakening of the easterly anomalies associated with the Kelvin wave leads to reduced zonal moisture advection, resulting in a moisture deficit in the MC boundary layer, thereby inhibiting the development of congestus convection. This suppression hinders vertical moisture transport to the mid-to-upper troposphere, preventing the establishment of the deep moist environment prerequisite for the onset of deep convection over the MC. Simultaneously, destructive interference from westward-propagating ER waves further exacerbates this suppression. Collectively, these processes result in the significant weakening of MJO convective activity as it traverses the MC, manifesting as the MC-PB phenomenon.

Discussion

The Madden–Julian Oscillation (MJO) drives improvements in subseasonal forecast skill, supporting preparedness for high-impact weather and enhancing the accuracy of short-term climate predictions. However, state-of-the-art numerical models generally suffer from a rapid decline in prediction skill when the MJO propagates across the Maritime Continent (MC), a phenomenon known as the Maritime Continent prediction barrier (MC-PB). While previous studies have predominantly attributed the MC-PB to model uncertainties, the potential for initial errors to induce the MC-PB has remained largely unexplored.

Based on an analysis of Subseasonal-to-Seasonal Prediction Project (S2S) ensemble hindcasts, this study reveals that for propagating MJO events observed to cross the MC, ensemble members exhibit divergent behaviors: some accurately predict the crossing, whereas others erroneously forecast the decay and dissipation of the MJO over the MC. Since these members differ solely in their initial conditions, this result indicates that initial uncertainty is a critical factor in triggering the MC-PB. This finding challenges the traditional perspective that attributes the MC-PB exclusively to model errors.

Furthermore, by applying the Conditional Nonlinear Optimal Perturbation (CNOP) method to four propagating MJO events simulated by the Community Earth System Model, version 1 (CESM1), this study identifies two distinct types of initial moisture errors that are particularly effective at inducing the MC-PB for the respective events. The first type is characterized by a zonal dipole pattern in the horizontal and a baroclinic structure in the vertical. This error triggers the MC-PB by decelerating the MJO eastward propagation via amplification of the westward-propagating equatorial Rossby (ER) wave. Specifically, the ER dry phase suppresses the MJO active phase over the MC, while its wet phase replaces the MJO suppressed phase over the Indian Ocean (IO). This asymmetric modulation leads to a significant phase lag in MJO propagation over the MC, ultimately triggering the MC-PB. The second type of initial moisture error manifests as a multipole structure with alternating positive and negative centers. This error triggers the MC-PB through two synergistic processes that weaken MJO intensity. On the one hand, by altering the structure and intensity of the ER wave train, it excites an eastward-dispersing disturbance wave train dominated by dry perturbations. This disturbance primarily dampens the MJO amplitude throughout its propagation, exerting a particularly strong suppression effect over the MC. On the other hand, weakening active convection in the Eastern Indian Ocean (EIO) diminishes the downstream equatorial Kelvin wave signal, leading to reduced zonal moisture advection and insufficient moisture supply over the MC, thereby inhibiting the initiation and development of new convection in this region. The combined effect of these two mechanisms causes the MJO to weaken markedly while traversing the MC, ultimately resulting in the MC-PB. Notably, compared to spatially random initial errors and initial perturbations from the NCEP ensemble prediction system, the CNOP-type errors exhibit significantly more coherent structures and concentrated energy, which likely makes them more effective at generating large forecast deviations and triggering a pronounced MC-PB. In fact, initial perturbations in the NCEP forecast system are generated using the lagged average forecast (LAF) method and therefore tend to be relatively diffuse and small-scale. This difference in perturbation characteristics may partly contribute to the relatively low ensemble spread (under-dispersion) reported in operational MJO forecasts[12], motivating future exploration of CNOP-based targeted perturbation strategies to enhance ensemble diversity and reliability.

This study underscores the important role of accurate initial conditions in alleviating the MC-PB effect. It provides new insights into the underlying mechanisms of this barrier and establishes a theoretical foundation for improving MJO prediction skill via optimized initialization strategies. Notably, our findings align with the event-oriented predictability perspective recently proposed by Liu et al.[60], which highlights the importance of event-specific dynamics in subseasonal forecast skill. Our results confirm the crucial role of nonlinearity, showing that initial error growth is flow-dependent and can produce the prediction barrier through event-dependent pathways. However, several limitations of this work should be acknowledged. Calculating CNOPs involves solving a high-dimensional optimization problem, which is computationally intensive within a complex coupled model. Therefore, this study focused on four representative propagating MJO events for the CNOP analysis. Nevertheless, the results from these numerical experiments are consistent with the statistical analysis of the S2S hindcasts, robustly demonstrating that initial errors alone are sufficient to trigger the MC-PB. In particular, the CNOP errors would cause the much more severe MC-PB, as compared with the initial errors of the S2S hindcasts. To further consolidate these findings, future work will employ a larger sample of MJO events, particularly realistic cases initialized via data assimilation. Moreover, the rapid advancement of machine learning models, which can operate with substantially lower computational cost, presents a promising opportunity to overcome the current computational bottlenecks and support broader sensitivity studies in future research. Furthermore, the detailed dynamical processes by which CNOP-type errors lead to the MC-PB warrant further investigation. For instance, it remains unclear through which physical processes the initial error enhances the westward-propagating ER wave in CASE1, and how it modulates the ER wave train and weakens convection over the EIO in CASE3. Furthermore, the MC features complex topography and a unique land-sea distribution that drives strong diurnal cycles, which may influence MJO propagation through local processes[20,61]. Current numerical models often fail to accurately capture these local processes, thereby introducing model errors. How initial errors and model errors interact to induce the MC-PB and affect MJO prediction skill remains an open question. Addressing these critical scientific issues will not only help build a comprehensive understanding of the causes of the MC-PB but also provide a solid theoretical foundation for developing advanced forecasting strategies to significantly enhance MJO prediction skill.

Data availability

The RMM indices utilized for the statistical analysis of S2S hindcasts are sourced from the Subseasonal-to-Seasonal Prediction project database at https://confluence.ecmwf.int/display/S2S/Tools. The model output data generated in this study are archived at the Beijing Super Cloud Computing Center (https://cloud.blsc.cn) and are available from the corresponding author upon reasonable request.

Code availability

The source codes for the analysis of this study are available from the corresponding authors upon reasonable request.

Received: 9 January 2026; Accepted: 25 February 2026;
Published online: 14 March 2026

References

1. Madden, R. A. & Julian, P. R. Detection of a 40–50 day oscillation in the zonal wind in the tropical Pacific. *J. Atmos. Sci.* **28**, 702–708 (1971).
2. Madden, R. A. & Julian, P. R. Description of global-scale circulation cells in the tropics with a 40–50 day period. *J. Atmos. Sci.* **29**, 1109–1123 (1972).
3. Liebmann, B., Hendon, H. H. & Glick, J. D. The relationship between tropical cyclones of the western Pacific and Indian Oceans and the Madden-Julian oscillation. *J. Meteorol. Soc. Jpn.* **72**, 401–412 (1994).
4. Maloney, E. D. & Hartmann, D. L. Modulation of eastern North Pacific hurricanes by the Madden–Julian oscillation. *J. Clim.* **13**, 1451–1460 (2000).
5. Jeong, J.-H., Kim, B.-M., Ho, C.-H. & Noh, Y.-H. Systematic variation in wintertime precipitation in East Asia by MJO-induced extratropical vertical motion. *J. Clim.* **21**, 788–801 (2008).
6. Jeong, J. H., Ho, C. H., Kim, B. M. & Kwon, W. T. Influence of the Madden-Julian Oscillation on wintertime surface air temperature and cold surges in East Asia. *J. Geophys. Res. Atmos.* **110**, D11 (2005).
7. Schreck, C. J. Global survey of the MJO and extreme precipitation. *Geophys. Res. Lett.* **48**, e2021GL094691 (2021).
8. Domeisen, D. I. et al. Advances in the subseasonal prediction of extreme events: relevant case studies across the globe. *Bull. Am. Meteorol. Soc.* **103**, E1473–E1501 (2022).
9. Chen, L. et al. A machine learning model that outperforms conventional global subseasonal forecast models. *Nat. Commun.* **15**, 6425 (2024).
10. Vitart, F. & Robertson, A. W. The sub-seasonal to seasonal prediction project (S2S) and the prediction of extreme events. *npj Clim. Atmos. Sci.* **1**, 3 (2018).
11. Wheeler, M. C. & Hendon, H. H. An all-season real-time multivariate MJO index: development of an index for monitoring and prediction. *Mon. Weather Rev.* **132**, 1917–1932 (2004).
12. Kim, H., Vitart, F. & Waliser, D. E. Prediction of the Madden–Julian oscillation: a review. *J. Clim.* **31**, 9425–9443 (2018).
13. Lim, Y., Son, S.-W. & Kim, D. MJO prediction skill of the subseasonal-to-seasonal prediction models. *J. Clim.* **31**, 4075–4094 (2018).
14. Neena, J. M., Lee, J. Y., Waliser, D., Wang, B. & Jiang, X. Predictability of the Madden–Julian oscillation in the intraseasonal variability hindcast experiment (ISVHE). *J. Clim.* **27**, 4531–4543 (2014).
15. Duan, W. et al. Recent advances in China on the predictability of weather and climate. *Adv. Atmos. Sci.* **40**, 1521–1547 (2023).
16. Inness, P. M. & Slingo, J. M. Simulation of the Madden–Julian oscillation in a coupled general circulation model. Part I: comparison with observations and an atmosphere-only GCM. *J. Clim.* **16**, 345–364 (2003).
17. Wang, W., Hung, M.-P., Weaver, S. J., Kumar, A. & Fu, X. MJO prediction in the NCEP Climate Forecast System version 2. *Clim. Dyn.* **42**, 2509–2520 (2014).
18. Xiang, B. et al. S2S prediction in GFDL SPEAR: MJO diversity and teleconnections. *Bull. Am. Meteorol. Soc.* **103**, E463–E484 (2022).
19. Gonzalez, A. O. & Jiang, X. Winter mean lower tropospheric moisture over the Maritime Continent as a climate model diagnostic metric for the propagation of the Madden-Julian oscillation. *Geophys. Res. Lett.* **44**, 2588–2596 (2017).
20. Peatman, S. C., Matthews, A. J. & Stevens, D. P. Propagation of the Madden–Julian Oscillation through the Maritime Continent and scale interaction with the diurnal cycle of precipitation. *Q. J. R. Meteorol. Soc.* **140**, 814–825 (2014).
21. Hagos, S. M. et al. The impact of the diurnal cycle on the propagation of Madden-Julian O scillation convection across the Maritime Continent. *J. Adv. Model. Earth Syst.* **8**, 1552–1564 (2016).
22. Baranowski, D. B., Waliser, D. E., Jiang, X., Ridout, J. A. & Flatau, M. K. Contemporary GCM fidelity in representing the diurnal cycle of precipitation over the Maritime Continent. *J. Geophys. Res. Atmos.* **124**, 747–769 (2019).
23. Inness, P. M. & Slingo, J. M. The interaction of the Madden–Julian oscillation with the Maritime Continent in a GCM. *Q. J. R. Meteorol. Soc.* **132**, 1645–1667 (2006).
24. Hsu, H.-H. & Lee, M.-Y. Topographic effects on the eastward propagation and initiation of the Madden–Julian oscillation. *J. Clim.* **18**, 795–809 (2005).
25. Wu, C.-H. & Hsu, H.-H. Topographic influence on the MJO in the Maritime Continent. *J. Clim.* **22**, 5433–5448 (2009).
26. Vitart, F. & Molteni, F. Simulation of the Madden–Julian oscillation and its teleconnections in the ECMWF forecast system. *Q. J. R. Meteorol. Soc.* **136**, 842–855 (2010).
27. Vitart, F., Woolnough, S., Balmaseda, M. & Tompkins, A. Monthly forecast of the Madden–Julian oscillation using a coupled GCM. *Mon. Weather Rev.* **135**, 2700–2715 (2007).
28. Fu, X. et al. Multi-model MJO forecasting during DYNAMO/CINDY period. *Clim. Dyn.* **41**, 1067–1081 (2013).
29. Liu, X. et al. MJO prediction using the sub-seasonal to seasonal forecast model of Beijing Climate Center. *Clim. Dyn.* **48**, 3283–3307 (2017).
30. Yao, J., Vitart, F., Balmaseda, M. A., Wu, T. & Liu, X. The impact of coupled data assimilation on Madden–Julian Oscillation predictability initialized from coupled satellite-era reanalysis. *Mon. Weather Rev.* **149**, 2897–2912 (2021).
31. Bengtsson, L. et al. The crucial role of the initial state in MJO prediction. *Geophys. Res. Lett.* **52**, e2025GL115833 (2025).
32. Takasuka, D., Suematsu, T., Miura, H. & Nakano, M. Propagation of the Madden-Julian oscillation as a deterministic chaotic phenomenon. *Sci. Adv.* **12**, eadz1916 (2026).
33. Mu, M., Duan, W. & Wang, B. Conditional nonlinear optimal perturbation and its applications. *Nonlinear Process. Geophys.* **10**, 493–501 (2003).
34. Li, X. et al. Assessment of Madden–Julian oscillation simulations with various configurations of CESM. *Clim. Dyn.* **47**, 2667–2690 (2016).
35. Richter, J. H. et al. Subseasonal prediction with and without a well-represented stratosphere in CESM1. *Weather Forecast* **35**, 2589–2602 (2020).
36. Hurrell, J. W. et al. The community earth system model: a framework for collaborative research. *Bull. Am. Meteorol. Soc.* **94**, 1339–1360 (2013).
37. Hudson, D., Marshall, A. G., Yin, Y., Alves, O. & Hendon, H. H. Improving intraseasonal prediction with a new ensemble generation strategy. *Mon. Weather Rev.* **141**, 4429–4449 (2013).
38. Saha, S. et al. The NCEP climate forecast system version 2. *J. Clim.* **27**, 2185–2208 (2014).
39. Gottschalck, J. et al. A framework for assessing operational Madden–Julian oscillation forecasts: a CLIVAR MJO working group project. *Bull. Am. Meteorol. Soc.* **91**, 1247–1258 (2010).
40. Wang, B., Chen, G. & Liu, F. Diversity of the Madden-Julian oscillation. *Sci. Adv.* **5**, eaax0220 (2019).
41. Jones, C., Hazra, A. & Carvalho, L. M. The Madden–Julian oscillation and boreal winter forecast skill: an analysis of NCEP CFSv2 reforecasts. *J. Clim.* **28**, 6297–6307 (2015).
42. Lafleur, D. M., Barrett, B. S. & Henderson, G. R. Some climatological aspects of the Madden–Julian Oscillation (MJO). *J. Clim.* **28**, 6039–6053 (2015).
43. Densmore, C. R., Sanabia, E. R. & Barrett, B. S. QBO influence on MJO amplitude over the Maritime Continent: physical mechanisms and seasonality. *Mon. Weather Rev.* **147**, 389–406 (2019).
44. Jiang, X. et al. Fifty years of research on the Madden-Julian Oscillation: recent progress, challenges, and perspectives. *J. Geophys. Res. Atmos.* **125**, e2019JD030911 (2020).
45. Wei, Y., Mu, M., Ren, H. L. & Fu, J. X. Conditional nonlinear optimal perturbations of moisture triggering primary MJO initiation. *Geophys. Res. Lett.* **46**, 3492–3501 (2019).

46. Wu, J. et al. Effects of moisture initialization on MJO and its teleconnection prediction in BCC subseasonal coupled model. *J. Geophys. Res. Atmos.* **125**, e2019JD031537 (2020).
47. Zeng, L. et al. Impacts of humidity initialization on MJO prediction: a study in an operational sub-seasonal to seasonal system. *Atmos. Res.* **294**, 106946 (2023).
48. Kim, D., Kim, H. & Lee, M. I. Why does the MJO detour the Maritime Continent during austral summer? *Geophys. Res. Lett.* **44**, 2579–2587 (2017).
49. Zhao, C., Li, T. & Zhou, T. Precursor signals and processes associated with MJO initiation over the tropical Indian Ocean. *J. Clim.* **26**, 291–307 (2013).
50. Dee, D. P. et al. The ERA-interim reanalysis: configuration and performance of the data assimilation system. *Q. J. R. Meteorol. Soc* **137**, 553–597 (2011).
51. Duchon, C. E. Lanczos filtering in one and two dimensions. *J. Appl. Meteorol* **18**, 1016–1022 (1979).
52. DeMott, C. A., Wolding, B. O., Maloney, E. D. & Randall, D. A. Atmospheric mechanisms for MJO decay over the Maritime Continent. *J. Geophys. Res. Atmos.* **123**, 5188–5204 (2018).
53. Wei, Y., Ren, H. L., Duan, W. & Sun, G. Westward-propagating disturbances shape diverse MJO propagation. *Geophys. Res. Lett.* **50**, e2023GL104778 (2023).
54. Wheeler, M. & Kiladis, G. N. Convectively coupled equatorial waves: analysis of clouds and temperature in the wavenumber–frequency domain. *J. Atmos. Sci.* **56**, 374–399 (1999).
55. Barrett, B. S., Densmore, C. R., Ray, P. & Sanabia, E. R. Active and weakening MJO events in the Maritime Continent. *Clim. Dyn.* **57**, 157–172 (2021).
56. Yanai, M., Esbensen, S. & Chu, J.-H. Determination of bulk properties of tropical cloud clusters from large-scale heat and moisture budgets. *J. Atmos. Sci.* **30**, 611–627 (1973).
57. Adames, ÁF. Precipitation budget of the Madden–Julian oscillation. *J. Atmos. Sci.* **74**, 1799–1817 (2017).
58. Hung, C.-S. & Sui, C.-H. A diagnostic study of the evolution of the MJO from Indian Ocean to Maritime Continent: wave dynamics versus advective moistening processes. *J. Clim.* **31**, 4095–4115 (2018).
59. Chen, G. & Wang, B. Effects of enhanced front Walker cell on the eastward propagation of the MJO. *J. Clim.* **31**, 7719–7738 (2018).
60. Liu, F. et al. Opportunities and barriers for skillful subseasonal prediction of East Asian summer precipitation. *Bull. Am. Meteorol. Soc.* **105**, E2216–E2230 (2024).
61. Zhang, C. & Ling, J. Barrier effect of the Indo-Pacific Maritime Continent on the MJO: perspectives from tracking MJO precipitation. *J. Clim.* **30**, 3439–3459 (2017).

Acknowledgements

This work was supported by the National Natural Science Foundation of China (Grant No. 42330111). The numerical experiments were supported by the National Key Scientific and Technological Infrastructure project "Earth System Numerical Simulation Facility" (EarthLab).

Author contributions

W.D., X.W., and Y.W. designed the research. W.D. and X.W. carried out the analyses. W.D. and Y.W. supervised the study. All authors wrote and revised the manuscript.

Competing interests

The authors declare no competing interests.

Additional information

Correspondence and requests for materials should be addressed to Wansuo Duan or Yuntao Wei.

Reprints and permissions information is available at http://www.nature.com/reprints

Publisher's note Springer Nature remains neutral with regard to jurisdictional claims in published maps and institutional affiliations.

Open Access This article is licensed under a Creative Commons Attribution-NonCommercial-NoDerivatives 4.0 International License, which permits any non-commercial use, sharing, distribution and reproduction in any medium or format, as long as you give appropriate credit to the original author(s) and the source, provide a link to the Creative Commons licence, and indicate if you modified the licensed material. You do not have permission under this licence to share adapted material derived from this article or parts of it. The images or other third party material in this article are included in the article's Creative Commons licence, unless indicated otherwise in a credit line to the material. If material is not included in the article's Creative Commons licence and your intended use is not permitted by statutory regulation or exceeds the permitted use, you will need to obtain permission directly from the copyright holder. To view a copy of this licence, visit http://creativecommons.org/licenses/by-nc-nd/4.0/.

© The Author(s) 2026